



HAL
open science

Dispersion-based intertwined SEIRA and SPR effect detection of 2,4-dinitrotoluene using a plasmonic metasurface

Alice Fabas, Hasnaa El Ouazzani, Jean-Paul Hugonin, Christophe Dupuis, Riad Haidar, Jean-Jacques Greffet, Patrick Bouchon

► **To cite this version:**

Alice Fabas, Hasnaa El Ouazzani, Jean-Paul Hugonin, Christophe Dupuis, Riad Haidar, et al.. Dispersion-based intertwined SEIRA and SPR effect detection of 2,4-dinitrotoluene using a plasmonic metasurface. *Optics Express*, 2020, 28 (26), pp.39595-39605. 10.1364/OE.413325 . hal-03116556

HAL Id: hal-03116556

<https://hal.science/hal-03116556>

Submitted on 20 Jan 2021

HAL is a multi-disciplinary open access archive for the deposit and dissemination of scientific research documents, whether they are published or not. The documents may come from teaching and research institutions in France or abroad, or from public or private research centers.

L'archive ouverte pluridisciplinaire **HAL**, est destinée au dépôt et à la diffusion de documents scientifiques de niveau recherche, publiés ou non, émanant des établissements d'enseignement et de recherche français ou étrangers, des laboratoires publics ou privés.



Dispersion-based intertwined SEIRA and SPR effect detection of 2,4-dinitrotoluene using a plasmonic metasurface

ALICE FABAS,¹ HASNA EL OUAZZANI,¹ JEAN-PAUL HUGONIN,²
CHRISTOPHE DUPUIS,³ RIAD HAIDAR,^{1,4} JEAN-JACQUES
GREFFET,²  AND PATRICK BOUCHON^{1,*} 

¹DOTA, ONERA, Université Paris-Saclay, 91123 Palaiseau, France

²Laboratoire Charles Fabry, Institut d'Optique Graduate School, CNRS, Université Paris-Saclay, 91127 Palaiseau, France

³Center for Nanosciences and Nanotechnology (C2N) - CNRS, Université Paris-Saclay, 10 Boulevard Thomas Gobert, 91120 Palaiseau, France

⁴Ecole polytechnique, Département de Physique, 91128 Palaiseau, France

*patrick.bouchon@onera.fr

Abstract: Surface enhanced infrared absorption (SEIRA) spectroscopy and surface plasmon resonance (SPR) make possible, thanks to plasmonics nanoantennas, the detection of low quantities of biological and chemical materials. Here, we investigate the infrared response of 2,4-dinitrotoluene deposited on various arrays of closely arranged metal-insulator-metal (MIM) resonators and experimentally show how the natural dispersion of the complex refractive index leads to an intertwined combination of SEIRA and SPR effect that can be leveraged to identify molecules. They are shown to be efficient for SEIRA spectroscopy and allows detecting of the dispersive explosive material, 2,4-dinitrotoluene. By changing the in-plane parameters, a whole spectral range of absorptions of 2,4-DNT is scanned. These results open the way to the design of sensors based on SEIRA and SPR combined effects, without including a spectrometer.

© 2020 Optical Society of America under the terms of the [OSA Open Access Publishing Agreement](#)

1. Introduction

Spectroscopy is a widely used technique to identify molecules thanks to their absorption wavelengths, which, each associated with a given bandwidth, are a unique and recognizable fingerprint of the molecules [1]. These absorption bands can be further increased if the molecules are placed in the neighborhood of a metallic surface or a resonant nanostructure that increases the electric field surrounding the targeted molecules [2]. This is referred in the community as surface enhanced infrared absorption spectroscopy (SEIRA), and its sensitivity not only depends on the molecule absorption peak and bandwidth, but also on its amplitude [3]. Chemical databases provide the absorption peaks and bandwidths for most molecules in the infrared, but not their amplitudes, which are paramount to the electromagnetic prediction and interpretation of SEIRA characterizations. Besides, variations of the refractive index are related to these absorption peaks through the Kramers Kronigs relations [4]. The refractive index itself is used to identify molecules thanks to surface plasmon resonance effects (SPR) [5], but targeted molecules have either a constant refractive index or a low-dispersion [6]. Another challenge that has restrained the practical use of SEIRA, is to identify a given molecule without an infrared spectrometer, for instance with a limited number of wavelengths.

One of the main focus of SEIRA studies has been to develop nanoantennas with the highest enhancement possible [7,8]. Many structures of various geometry exhibiting very high electric field enhancement have been developed: nanorods [9–12], optical split-ring [13], fan-shaped antennas [14], crosses-shaped antennas [15,16]. Nevertheless, these high enhancement factors

are concentrated at the antennas' tips and only have a small spatial extension in hot spots, whereas both the enhancement and the volume of interaction are of importance. In contrast, metal-insulator-metal (MIM) resonators can enhance light on larger volumes. These MIM antenna have been widely studied in the past decade, a wide variety of shapes and materials have been investigated [17–20]. For instance, MIM nanoslits have been used to increase the SEIRA signal of the commonly used Octadecanethiol (ODT), a self-assembling molecule monolayer with a thiol group that binds to a metallic surface [11,21]. Buried plasmonic cavities were shown to achieve absorption variations up to 20% and sub-10 nm nanogaps have recently been shown to achieve similar results with a 5 nm thick silk fibroin molecules [22,23]. MIM nanopatches have also been used to enhance the SEIRA signal of dodecanethiol, a molecule with properties close to ODT [24]. This geometry main advantage is its simplicity of fabrication, but the SEIRA signal remains below 5%.

In this paper, we study the infrared response of 2,4-dinitrotoluene deposited on various arrays of closely arranged MIM resonators, and experimentally show how the natural dispersion of the complex refractive index leads to an intertwined combination of SEIRA and SPR effect that can be leveraged to identify molecules. First, this specific resonator geometry exhibits a high and homogeneous enhancement factor in the whole volume of its slits, which can be increased as well as the resulting SEIRA signal without significant change of the enhancement factor. The experimental study of the resonator shows a near total absorption with a good angular stability. Then, the structure is applied to the detection of a nitrosaromatic molecule, 2,4-dinitrotoluene (2,4-DNT). A model of permittivity of this molecule is developed in order to simulate the response of the system. Finally, we also take advantage of the ability to adjust the resonant wavelength by simply changing the in plane parameters of the MIM resonator to introduce a multiple resonator device, which could be used in a more sophisticated sensor to increase the specificity of detection, thus decreasing false alarms.

2. Computational study

2.1. Enhancement factor computations

The structure is depicted in Fig. 1(a), it is based on a gold-silica-gold stack where only the top metallic layer is periodically patterned in one direction (period d). MIM resonators are usually well separated to avoid near-field coupling and take advantage of their large cross section [25–27]. Here, we use ribbons which are closely arranged so that the system can be viewed as a periodic array of slits (height h_s and width w_s) above the dielectric layer (height h_b). The bottom gold layer is thick enough to be optically opaque. Light is incoming on the structure with a polarization such that the magnetic field component $H_x = 0$, which corresponds to the TM-polarization for a null azimuth angle ($\phi = 0^\circ$).

Maxwell's equations are solved using a B-splines modal method [28] which have also been compared with a rigorous coupled wave analysis method [29]. The material used in the metallic parts is gold whose permittivity is given by the following Drude model in agreement with experimental data in the infrared range: $\epsilon_{Au}(\lambda) = 1 - 1/(\lambda_p/\lambda(\lambda_p/\lambda + i\gamma))$ with $\lambda_p = 159$ nm and $\gamma = 0.0075$ [30]. The computational results are made in TM polarization and at normal incidence : $\theta = \phi = 0^\circ$. Thus, as shown in Fig. 1(a), the magnetic field is oriented along the slits.

Figure 1(b) shows the spectrum of the mean enhancement of the electric field intensity inside the slit volume for a resonator whose geometric dimensions are: $d = 1.5 \mu\text{m}$, $h_s = 60$ nm, $w_s = 50$ nm, $h_b = 50$ nm and whose cavity is filled with a dielectric of constant permittivity $\epsilon_b = 2$. The highest mean enhancement is reached at $\lambda_r = 6.82 \mu\text{m}$ and reaches $|E/E_0|^2 = 1.07 \times 10^3$. As shown on the map of the electric field intensity on Fig. 1(d) at λ_r , this mean value is actually very close to the enhancement factor anywhere in the slit. In fact, the magnetic field is enhanced in the dielectric layer (data not shown), so the resonance is not due to the slit alone. These closely arranged MIM can be described as an LC resonator: the electric field is concentrated in the slit

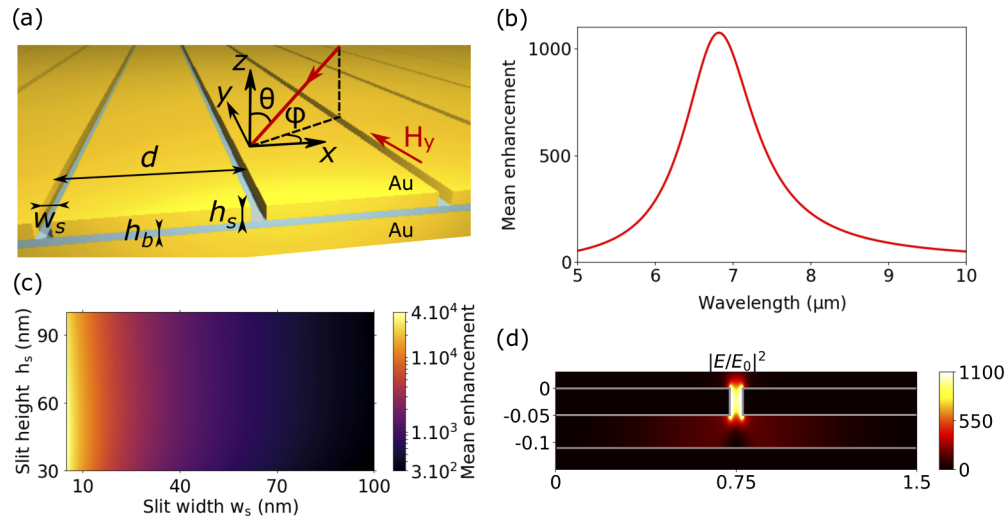


Fig. 1. (a) 3D-scheme of the MIM resonator (period d), made of a slit (height h_s , width w_s) atop a dielectric layer (height h_b) and a gold mirror. The structure is invariant along the y -axis. (b) Mean enhancement spectrum inside the volume of the slit, at normal incidence in TM polarization, of a resonator whose dimensions are: $d = 1.5 \mu\text{m}$, $h_s = 50 \text{ nm}$, $w_s = 50 \text{ nm}$ and $h_b = 60 \text{ nm}$ and with a constant permittivity of the dielectric layer: $\epsilon_b = 2$. (c) Mean enhancement in the slit volume at the resonance wavelength of a MIM resonator as a function of its slit width w_s and height h_s . The other parameters are: $d = 1.5 \mu\text{m}$, $h_b = 60 \text{ nm}$ and $\epsilon_b = 2$. A normal-incident wave with TM-polarization is used. (d) Map of the electric field intensity inside the structure whose spectrum is shown on (b) at the resonance $\lambda_r = 6.82 \mu\text{m}$.

which acts like a capacitor and the magnetic field is in the dielectric cavity that can be considered like an inductance. All the geometric parameters have an influence on the resonance wavelength, so that various sets of geometric parameters can lead to the same resonance wavelength.

Although the enhancement of the electric field is lower than those reported in the literature [14], it is homogeneous in a large volume and not only in hot spots. The enhancement reached is similar to those observed in tip-to-tip dimer nanoantennas with gaps of the same size [31], but which are not infinite along one direction, thus limiting the enhancement volume. It is also of the same order as the intensity in gold cross antenna, whose, spatial extension is limited to the gap between the cross arms (approximately $40 \times 40 \text{ nm}^2$) [15]. Moreover, a relatively high enhancement factor, higher than 560, is reached on a large spectral range, with a full width at half maximum of $\text{FWHM} = 1.05 \mu\text{m}$. This enables the enhancement of spectrally close vibrational absorption lines with only one resonator. Both the spatial and the spectral extensions of the electric field enhancement are particularly appealing when it comes to sensors application as the effective area and bandwidth are widely increased.

The influence of the volume of the slit on the enhancement factor at resonance is now investigated. The impact of both the width and the height are shown on Fig. 1(c), whereas the other parameters are set to $d = 1.5 \mu\text{m}$, $h_b = 60 \text{ nm}$ and $\epsilon_b = 2$. As the slit is tightened, the enhancement soars, which can be attributed to the funneling effect [25,27,32–34]: all the incoming light goes through the narrow aperture which induces a d/w enhancement factor. For the tightest case ($w_s = 5 \text{ nm}$), almost a 4×10^4 enhancement is reached. On the opposite, the slit height has nearly no influence on the enhancement value. Typically, when the slit height h_s is increased from 30 nm to 100 nm , it leads to a 10% decrease. Thus, the enhancement intensity can be driven by the slit width, and since the enhancement is homogeneous in the slit, its volume can be tuned with its height without impairing the enhancement.

2.2. Absorption study

The reflectivity of the previous structure is shown on Fig. 2 (blue line). It exhibits a total absorption at $\lambda_r = 6.82 \mu\text{m}$. Its slit is then filled up with a material of complex permittivity in order to model its dispersive optical behaviour. The permittivity of this material is based on a Drude-Lorentz oscillator model:

$$\epsilon(\omega) = \epsilon_\infty + \sum_n A_n \frac{\omega_{0,n}^2}{(\omega_{0,n}^2 - \omega^2) - i\gamma_n\omega}. \quad (1)$$

Each absorption is modelled by an oscillator defined by its amplitude A_n , its eigenfrequency $\omega_{0,n}$ and its damping factor γ_n . For the sake of simplicity, only one absorption line will be considered here. Hence, $n = 1$, and the parameters are chosen as $\epsilon_\infty = 2.18$, $A_1 = 10^{-2}$, $\gamma_1 = 20 \text{ cm}^{-1}$, $\omega_{0,1} = 1348 \text{ cm}^{-1}$. The response of the MIM resonator whose slit is filled with this material is also shown on Fig. 2 (red curve). First, it is red-shifted compared to the empty case. It can be understood as a SPR effect due to the real part of the permittivity. Also, the absorption that matches the resonance appears, which characterizes the SEIRA phenomenon. The response of the resonator to molecules can be separated between the SPR effect and the SEIRA effect. To illustrate this, the response of the resonator where ϵ_∞ is set to one is shown (purple curve), as well as the case where only the real part of the permittivity is taken into account (orange curve). In the first case, the resonance wavelength is not shifted and both curves are similar apart from the absorption dip at $\lambda = 7.5 \mu\text{m}$. In the latter case, only the SPR effect remains and the resonance curve is shifted from $\Delta\lambda = 520 \text{ nm}$. In molecules, both effects are combined, and near an absorption of the molecule, the real part of the permittivity is dispersive. To identify a given molecule, not only have these effects to be accounted for, but they can be used to improve this identification.

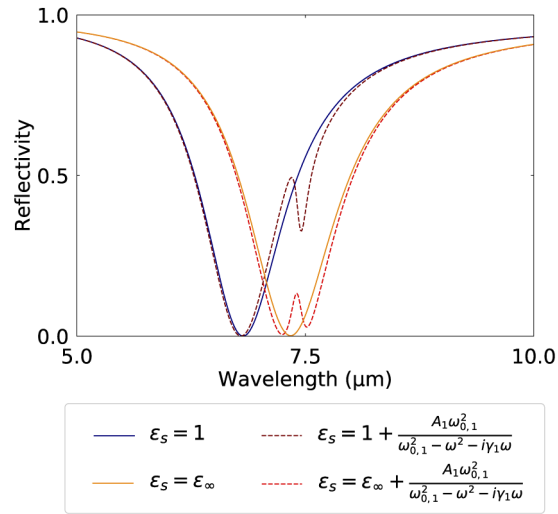


Fig. 2. Reflectivity spectra of the resonator ($d = 1.5 \mu\text{m}$, $w_s = 50 \text{ nm}$, $h_s = 50 \text{ nm}$, $h_b = 60 \text{ nm}$ and $\epsilon_b = 2$) whose slit is filled with materials of different permittivity, either with complex or real value. The incident light is normal to the surface and TM-polarized. The constant values are defined as: $\epsilon_\infty = 2.18$, $A_1 = 10^{-2}$, $\omega_{0,1} = 1348 \text{ cm}^{-1}$ and $\gamma_1 = 20 \text{ cm}^{-1}$.

3. Experimental demonstration

In order to demonstrate experimentally the ability of the large volume enhancement resonators to be used for SEIRA, we designed structures whose resonance matches the so-called *fingerprint region* between $5\ \mu\text{m}$ and $10\ \mu\text{m}$, which contains the main vibrational absorptions. The cavity layer of the resonator is filled with SiO_2 , whose permittivity is known from a Brendel-Bormann model [35].

The fabricated resonator consists of a stack of a gold layer and a SiO_2 layer (60 nm) separated by a thin chromium adhesion layer of 5 nm. Then, the 95 nm patterned top gold layer (with a 5 nm chromium adhesion layer) was obtained by an electron beam lithography and a lift-off. Thus, the total height of the slit is 100 nm. Two SEM (Scanning Electron Microscope) images of the sample are shown on Fig. 3(a).

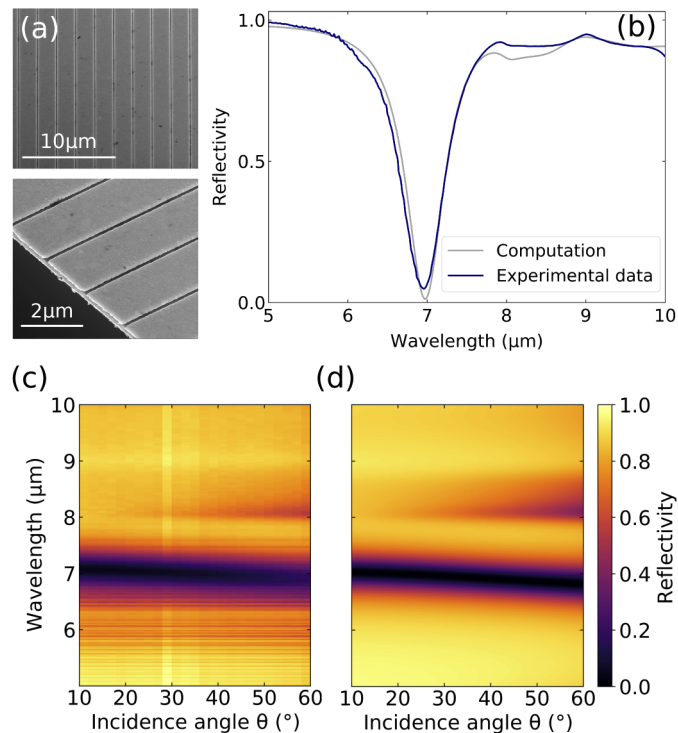


Fig. 3. (a) SEM images of a sample whose resonator dimensions are $d = 2.0\ \mu\text{m}$, $w_s = 125\ \text{nm}$, $h_b = 60\ \text{nm}$, $h_s = 95\ \text{nm}$, filled with SiO_2 and with 5 nm chromium adhesion layers. (b) Experimental response of a resonator (blue line) compared to its simulation spectrum (grey line). The incoming light is TM-polarized with incident angles between 12° and 24° , for all planes of incidence (ϕ between 0° and 360°). (c-d) Experimental and theoretical reflectivity map of the ribbon resonator as a function of the incident angle in TM polarization.

The experimental characterization is performed with a Bruker Vertex 70 Fourier Transform Infrared (FTIR) spectrometer, coupled with a Bruker Hyperion 2000 microscope with a Cassegrain objective ($NA = 0.4$). The measurements are done using the internal mid-infrared source of the spectrometer and an InSb photodetector. A square area of $100\ \mu\text{m} \times 100\ \mu\text{m}$ is imaged and the incident beam is linearly polarized with the magnetic field along the slits.

The experimental reflectivity spectrum is presented on Fig. 3(b). The main resonance appears at $\lambda_r = 6.97\ \mu\text{m}$ with a nearly total absorption of light. A fair agreement is found between

experimental data and simulation of a resonator under a beam focused by a Cassegrain objective. It is practically modelled by integrating calculations for TM-polarized incident light, with incident angles between 12° and 24° , for all planes of incidence (ϕ between 0° and 360°) and as in the experimental protocol, divided by the reflectivity of a gold layer with the same integration parameters. The chromium permittivity is modeled following a Brendel-Bormann model [36].

Finally, Figs. 3(c) and (d) shows experimentally and theoretically the angular dependence of the resonance, The experimental angular pattern is obtained using a goniometer setup coupled to the FTIR source, and is in very good agreement with the theoretical one. The main resonance at $\lambda_r = 6.97 \mu\text{m}$ appears to weakly depend on the incident angle of the incoming wave and its absorption is almost total up to 60° . This angular stability is very appealing when it comes to the integration of such a resonator in a whole optical set-up.

4. Permittivity model of 2,4-DNT

These large volume enhancement resonators are now applied to detection of 2,4-dinitrotoluene (shortly 2,4-DNT). This molecule is a precursor of the widespread explosive 2,4,6-trinitrotoluene (TNT). Thus, the detection of traces of 2,4-DNT indicates the presence of TNT [37]. The main techniques studied for the detection of this material are ion mobility spectroscopy and mass spectroscopy, which are limited by their cost and the selectivity they offer [38]. Optical techniques such as cavity ringdown spectroscopy [38] and Surface Plasmon Resonance (SPR) sensing [39] have also been developed. Here, we propose to study the ability of SEIRA to detect 2,4-DNT. Unlike, self-assembly monolayers of octadecanethiol that are often used as proof of concept in SEIRA studies [40,41], 2,4-DNT does not have specific affinity with the gold surface. This feature makes its use and detection quite challenging.

We first develop a model for the dielectric permittivity of 2,4-DNT in order to know the optical features of this material. It is based on the Drude-Lorentz model described by Eq. (1). In order to find the set of parameters ($\omega_{0,n}$, A_n , γ_n) and ϵ_∞ , absorption spectra of 2,4-DNT have been measured.

Table 1. Set of parameters ($\omega_{0,n}$, A_n , γ_n) for the Lorentz model of permittivity of 2,4-DNT, obtained by fitting experimental data.

n	$\omega_{0,n}$ (cm ⁻¹)	A_n	γ_n (cm ⁻¹)
1	1037	4.88×10^{-4}	15
2	1067	7.25×10^{-4}	10
3	1135	2.83×10^{-4}	11
4	1151	4.78×10^{-4}	9
5	1205	2.63×10^{-4}	15
6	1268	3.17×10^{-4}	12
7	1348	1.0×10^{-2}	20
8	1383	5.8×10^{-4}	15
9	1397	5.4×10^{-4}	15
10	1440	1.36×10^{-4}	10
11	1455	1.13×10^{-4}	10
12	1474	3.5×10^{-5}	10
13	1522	3.1×10^{-3}	23
14	1538	7.4×10^{-3}	22
15	1603	7.8×10^{-4}	15
16	1610	1.68×10^{-3}	15

The experimental data are collected thanks to a Fourier transform infrared spectrometer (FTIR, Bruker 70v). A few milligrams of solid 2,4-DNT are dissolved in acetonitrile. Some droplets of the solution, of a total volume of a tenth of microliter, are then dropped off on a gold mirror thanks to an air displacement pipette. The acetonitrile evaporates in a minute so only 2,4-DNT remains on the surface. The sample is studied in a reflection setup, in the both Transverse Magnetic (TM) and Transverse Electric (TE) incident polarizations, for different incident angles θ between 13° and 60° . All the absorptions are identified and associated to the vibration of a molecular group thanks to [37,42]. The match between computations and experimental data is made thanks to the method of the least squares. The thickness of the 2,4-DNT layer is estimated at $h = 1.9 \mu\text{m}$. The valuation of the set of parameters $(\omega_{0,n}, A_n, \gamma_n)$ is reported in the following Table 1. We estimate $\epsilon_\infty = 2.18$.

Thus, a permittivity model for 2,4-DNT is established. The both real and imaginary part of the refractive index, as $\tilde{n} = n + iK$, are shown on Fig. 4. Many absorptions are visible in the $5 - 10 \mu\text{m}$ range. We will focus on the most intense, namely ω_7 , ω_{14} and ω_{16} , between $6 \mu\text{m}$ and $8 \mu\text{m}$. They do not overlap with the absorptions of SiO_2 between $8 - 12 \mu\text{m}$.

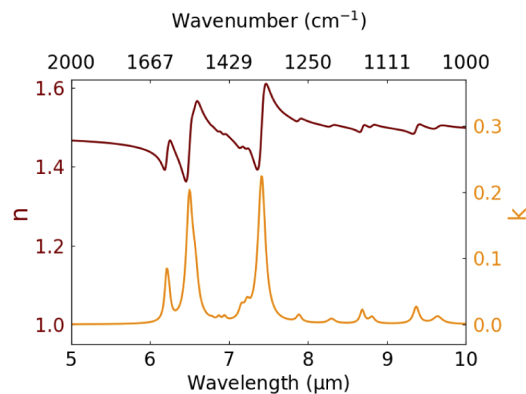


Fig. 4. Real (n) and imaginary (k) part of the refractive index of 2,4-DNT as a function of the wavelength, based on experimental data.

5. Detection of 2,4-DNT

A droplet of $5 \mu\text{L}$ of the solution of 2,4-DNT in acetonitrile was put on the resonator. After evaporation of the acetonitrile, 2,4-DNT is filling the slits, and there is an homogeneous 2,4-DNT layer on top of the metallic ribbons. The response was measured thanks to the Bruker Vertex 70 FTIR spectrometer with the Hyperion microscope, in the same experimental conditions as previously.

Figures 5(a)-(i) shows experimental spectra of nine different resonators of different dimensions (blue lines). As they were fabricated on the same wafer, the layer thicknesses are the same for every resonator: $h_b = 60 \text{ nm}$, $h_s = 95 \text{ nm}$ and a 5 nm chromium layer is used for adhesion. The resonance wavelength is tuned with the in plane parameters (w_s and d) so that the whole spectral range between $6 \mu\text{m}$ and $8 \mu\text{m}$ is covered.

As the 2,4-DNT material is deposited on the resonator, two phenomena can be observed on the red curves on Figs. 5(a)-(i). The first one is the redshift of the absorption of the resonator. It can be explained by a change of the real part of the refractive index inside the slit of the resonator, which is higher than 1 (shown on Fig. 4). Besides, as the resonance of the samples matches with 2,4-DNT vibrational absorptions, these absorptions appear on the spectrum of the structure. It illustrates the SEIRA mechanism that occurs here. The three main absorptions ω_7 , ω_{14} and ω_{16}

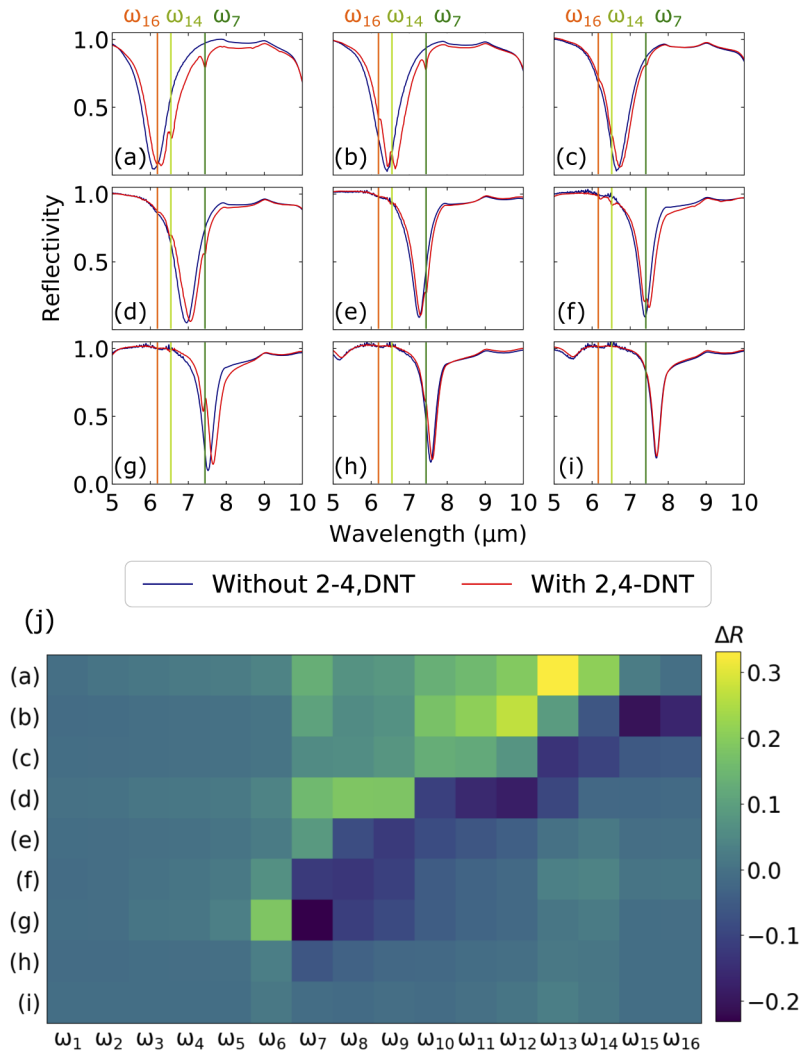


Fig. 5. (a-i) Experimental reflectivity response of nine different resonators without (blue line) and with 2,4-DNT in TM polarization. Layers heights are constant : $h_b = 60$ nm and $h_s = 95$ nm. The dielectric layer is made of SiO_2 and surrounded by 5 nm chromium adhesion layers. The periods d are : (a-d) $d = 2.0 \mu\text{m}$, (e-g) $d = 2.5 \mu\text{m}$, (h-i) $d = 3.0 \mu\text{m}$, and the slit widths w_s : (a,h) $w_s = 440$ nm, (b,e) $w_s = 345$ nm, (c,f,i) $w_s = 230$ nm and (d,g) $w_s = 125$ nm. (j) Difference of reflectivity of the 9 structures (a-i) at the main absorption wavelengths of 2,4-DNT.

can be seen in Figs. 5(a)-(g). It shows that the detection of 2,4-DNT with SEIRA is possible even though the molecule has no affinity with the surface and no functionalization was used. However, the spectra Fig. 5(i) are identical as they do not overlap any high intensity absorptions. The broadband feature of these structures that has been pointed out above can also be seen, with the enhancement of different absorptions on Figs. 5(a)-(d).

It is important to avoid the use of a spectrometer to reduce the size and price of a sensing device. Thus, we can think of measuring the reflectivity difference between the both without and with 2,4-DNT configurations at the absorption frequencies of the molecule, for panel of resonators covering the range of its absorptions. This is shown on Fig. 5(j) for the nine resonators of Figs. 5(a)-(i). This array shape makes it possible to detect both the SEIRA and SPR effects, and allows identifying it. On closer inspection, ω_7 appears to be better detected by resonators (f) and (g), ω_{14} by (a-c) and ω_{16} by (b). Each column offers a different response, insuring to bring specific information. Note that some resonators do not detect some lines: ω_{16} for (a) and ω_{14} for (b). Nevertheless, these main three absorptions are detected by other resonators with spectrally close resonance, with ΔR intensities that can be very high : for (f), whose resonance matches with ω_7 , $\Delta R = 0.12$. We must emphasize that these large differences are not obtained after a post-treatment of measurements but from direct comparison of the signals, backgrounded by a gold reference signal. Finally, as it has been pointed out before, the absorptions from ω_1 to ω_6 are not visible, as they overlap the absorption of SiO_2 and have a weak intensity. This array setup paves the way to the design of a cheap and portable devices, by adding a few additional resonators. It echoes the molecular barcoding proposed by Tittl and co-authors [43].

These data can difficultly be compared with the literature as 2,4-DNT and other explosive materials have not been investigated in SEIRA set-up so far. They can be approached by computations thanks to the permittivity model shown above. The slit must be filled with 2,4-DNT. The quantity of molecules in the active area of the slit is estimated at the picogram range for an extension along the y -axis of $30\ \mu\text{m}$. The material put on the ribbon is not taken into account as its contribution to the SEIRA signal is negligible. Nevertheless, this value does not represent the detection limit of our device as high differences of reflectivity are observed. Our work shows that an application of such a technique to the detection of traces of explosive materials is possible, with a simple experimental setup.

6. Conclusion

As a conclusion, we demonstrate the use of closely arranged MIM resonators to detect 2,4-DNT. The geometry considered offers very high enhancements, in the whole volume of the slits. These enhancements are of the same order of magnitude as the ones reported in the literature for the same spatial extension, but add a component along the y -axis. They can be increased by tightening the slit, but a trade-off between enhancement factor and effective section must be made. The resonators have been fabricated, and their characterization points out a very good angular stability, on a range of incidence angles up to 60° . They are finally applied to the detection of 2,4-DNT, whose optical response is investigated. By varying the in-plane parameters, an array of resonators covering the range of molecular absorptions can be made. Thus, scanning few frequencies that matches 2,4-DNT absorptions makes possible to identify the molecule, analysing both of the SEIRA and SPR effects. This setup offers a sketch for a sensor of dispersive materials based on SEIRA spectroscopy, combined to SPR and without including any spectrometer. It broadens the range of possibilities for the application of SEIRA-based sensors, allowing the detection of many different chemical and biological materials with a cost-reduced device.

Funding

Agence Nationale de la Recherche (ANR-16-CE39-0007).

Disclosures

The authors declare that there are no conflicts of interest related to this article.

References

1. B. Stuart, *Infrared Spectroscopy* (John Wiley & Sons Ltd., 2015), pp. 1–18.
2. M. Osawa, *Surface-Enhanced Infrared Absorption* (Springer Berlin Heidelberg, 2001), pp. 163–187.
3. S.-H. Oh and H. Altug, “Performance metrics and enabling technologies for nanoplasmonic biosensors,” *Nat. Commun.* **9**(1), 5263 (2018).
4. A. Kuzmenko, “Kramers–krönig constrained variational analysis of optical spectra,” *Rev. Sci. Instrum.* **76**(8), 083108 (2005).
5. K. A. Willets and R. P. Van Duyne, “Localized surface plasmon resonance spectroscopy and sensing,” *Annu. Rev. Phys. Chem.* **58**(1), 267–297 (2007).
6. Z.-M. Qi, M. Wei, H. Matsuda, I. Honma, and H. Zhou, “Broadband surface plasmon resonance spectroscopy for determination of refractive-index dispersion of dielectric thin films,” *Appl. Phys. Lett.* **90**(18), 181112 (2007).
7. F. Neubrech, C. Huck, K. Weber, A. Pucci, and H. Giessen, “Surface-enhanced infrared spectroscopy using resonant nanoantennas,” *Chem. Rev.* **117**(7), 5110–5145 (2017).
8. T. G. Mayerhöfer and J. Popp, “Periodic array-based substrates for surface-enhanced infrared spectroscopy,” *Nanophotonics* **7**(1), 39–79 (2018).
9. F. Neubrech, A. Pucci, T. W. Cornelius, S. Karim, A. García-Etxarri, and J. Aizpurua, “Resonant plasmonic and vibrational coupling in a tailored nanoantenna for infrared detection,” *Phys. Rev. Lett.* **101**(15), 157403 (2008).
10. C. D’Andrea, J. Bochterle, A. Toma, C. Huck, F. Neubrech, E. Messina, B. Fazio, O. M. Marago, E. Di Fabrizio, M. Lamy de La Chapelle, P. G. Gucciardi, and A. Pucci, “Optical nanoantennas for multiband surface-enhanced infrared and raman spectroscopy,” *ACS Nano* **7**(4), 3522–3531 (2013).
11. C. Huck, J. Vogt, M. Sendner, D. Hengstler, F. Neubrech, and A. Pucci, “Plasmonic enhancement of infrared vibrational signals: nanoslits versus nanorods,” *ACS Photonics* **2**(10), 1489–1497 (2015).
12. K. Weber, M. L. Nesterov, T. Weiss, M. Scherer, M. Hentschel, J. Vogt, C. Huck, W. Li, M. Dressel, H. Giessen, and F. Neubrech, “Wavelength scaling in antenna-enhanced infrared spectroscopy: Toward the far-IR and THz region,” *ACS Photonics* **4**(1), 45–51 (2017).
13. E. Cubukcu, S. Zhang, Y. S. Park, G. Bartal, and X. Zhang, “Split ring resonator sensors for infrared detection of single molecular monolayers,” *Appl. Phys. Lett.* **95**(4), 043113 (2009).
14. L. V. Brown, X. Yang, K. Zhao, B. Y. Zheng, P. Nordlander, and N. J. Halas, “Fan-shaped gold nanoantennas above reflective substrates for surface-enhanced infrared absorption (SEIRA),” *Nano Lett.* **15**(2), 1272–1280 (2015).
15. L. V. Brown, K. Zhao, N. King, H. Sobhani, P. Nordlander, and N. J. Halas, “Surface-enhanced infrared absorption using individual cross antennas tailored to chemical moieties,” *J. Am. Chem. Soc.* **135**(9), 3688–3695 (2013).
16. B. Cerjan, X. Yang, P. Nordlander, and N. J. Halas, “Asymmetric Aluminum Antennas for Self-Calibrating Surface-Enhanced Infrared Absorption Spectroscopy,” *ACS Photonics* **3**(3), 354–360 (2016).
17. Y. Cui, Y. He, Y. Jin, F. Ding, L. Yang, Y. Ye, S. Zhong, Y. Lin, and S. He, “Plasmonic and metamaterial structures as electromagnetic absorbers,” *Laser Photonics Rev.* **8**(4), 495–520 (2014).
18. R. Smaali, F. Omeis, A. Moreau, T. Taliercio, and E. Centeno, “A universal design to realize a tunable perfect absorber from infrared to microwaves,” *Sci. Rep.* **6**(1), 32589 (2016).
19. L. Li, S. Wu, L. Li, Z. Zhou, H. Ding, C. Xiao, and X. Li, “Gap-mode excitation, manipulation, and refractive-index sensing application by gold nanocube arrays,” *Nanoscale* **11**(12), 5467–5473 (2019).
20. L. Qin, S. Wu, J.-H. Deng, L. Li, and X. Li, “Tunable light absorbance by exciting the plasmonic gap mode for refractive index sensing,” *Opt. Lett.* **43**(7), 1427–1430 (2018).
21. R. Knipper, V. Kopecky Jr, U. Huebner, J. Popp, and T. G. Mayerhöfer, “Slit-enhanced chiral-and broadband infrared ultra-sensing,” *ACS Photonics* **5**(8), 3238–3245 (2018).
22. X. Chen, C. Ciraci, D. R. Smith, and S.-H. Oh, “Nanogap-enhanced infrared spectroscopy with template-stripped wafer-scale arrays of buried plasmonic cavities,” *Nano Lett.* **15**(1), 107–113 (2015).
23. D. Yoo, D. A. Mohr, F. Vidal-Codina, A. John-Herpin, M. Jo, S. Kim, J. Matson, J. D. Caldwell, H. Jeon, N.-C. Nguyen, L. Martin-Moreno, J. Peraire, H. Altug, and S.-H. Oh, “High-contrast infrared absorption spectroscopy via mass-produced coaxial zero-mode resonators with sub-10 nm gaps,” *Nano Lett.* **18**(3), 1930–1936 (2018).
24. J. Srajer, A. Schwaighofer, G. Ramer, S. Rotter, B. Guenay, A. Kriegner, W. Knoll, B. Lendl, and C. Nowak, “Double-layered nanoparticle stacks for surface enhanced infrared absorption spectroscopy,” *Nanoscale* **6**(1), 127–131 (2014).
25. P. Chevalier, P. Bouchon, R. Haïdar, and F. Pardo, “Funneling of light in combinations of metal-insulator-metal resonators,” *J. Nanophotonics* **6**(1), 063534 (2012).
26. C. Koechlin, P. Bouchon, F. Pardo, J.-L. Pelouard, and R. Haïdar, “Analytical description of subwavelength plasmonic mim resonators and of their combination,” *Opt. Express* **21**(6), 7025–7032 (2013).
27. P. Zhu, P. Jin, H. Shi, and L. J. Guo, “Funneling light into subwavelength grooves in metal/dielectric multilayer films,” *Opt. Express* **21**(3), 3595–3602 (2013).
28. P. Bouchon, F. Pardo, R. Haïdar, and J.-L. Pelouard, “Fast modal method for subwavelength gratings based on b-spline formulation,” *J. Opt. Soc. Am. A* **27**(4), 696–702 (2010).

29. J.-P. Hugonin and P. Lalanne, "Reticolo software for grating analysis," Inst. d'Optique, Palaiseau, France (2005).
30. E. Palik and G. Ghosh, *Handbook of optical constants of solids* (Academic, 1985).
31. C. Huck, F. Neubrech, J. Vogt, A. Toma, D. Gerbert, J. Katzmann, T. Härtling, and A. Pucci, "Surface-enhanced infrared spectroscopy using nanometer-sized gaps," *ACS Nano* **8**(5), 4908–4914 (2014).
32. P. Bouchon, F. Pardo, B. Portier, L. Ferlazzo, P. Ghenuche, G. Dagher, C. Dupuis, N. Bardou, R. Häïdar, and J. L. Pelouard, "Total funneling of light in high aspect ratio plasmonic nanoresonators," *Appl. Phys. Lett.* **98**(19), 191109 (2011).
33. F. Pardo, P. Bouchon, R. Häïdar, and J.-L. Pelouard, "Light funneling mechanism explained by magnetoelectric interference," *Phys. Rev. Lett.* **107**(9), 093902 (2011).
34. D. Adams, S. Inampudi, T. Ribaudo, D. Slocum, S. Vangala, N. Kuhta, W. Goodhue, V. A. Podolskiy, and D. Wasserman, "Funneling light through a subwavelength aperture with epsilon-near-zero materials," *Phys. Rev. Lett.* **107**(13), 133901 (2011).
35. J. Kischkat, S. Peters, B. Gruska, M. Semtsiv, M. Chashnikova, M. Klinkmüller, O. Fedosenko, S. Machulik, A. Aleksandrova, G. Monastyrskyi, Y. Flores, and W. T. Masselink, "Mid-infrared optical properties of thin films of aluminum oxide, titanium dioxide, silicon dioxide, aluminum nitride, and silicon nitride," *Appl. Opt.* **51**(28), 6789–6798 (2012).
36. A. D. Rakić, A. B. Djurišić, J. M. Elazar, and M. L. Majewski, "Optical properties of metallic films for vertical-cavity optoelectronic devices," *Appl. Opt.* **37**(22), 5271–5283 (1998).
37. A. Puiu, G. Giubileo, S. N. Cesaro, and L. Bencivenni, "Comprehensive Infrared Study of Tetryl, Dinitrotoluene, and Trinitrotoluene Compounds," *Appl. Spectrosc.* **69**(12), 1472–1486 (2015).
38. M. Snels, T. Venezia, and L. Belfiore, "Detection and identification of TNT, 2, 4-DNT and 2, 6-DNT by near-infrared cavity ringdown spectroscopy," *Chem. Phys. Lett.* **489**(1-3), 134–140 (2010).
39. K. Nagatomo, T. Kawaguchi, N. Miura, K. Toko, and K. Matsumoto, "Development of a sensitive surface plasmon resonance immunosensor for detection of 2,4-dinitrotoluene with a novel oligo (ethylene glycol)-based sensor surface," *Talanta* **79**(4), 1142–1148 (2009).
40. D. Enders and A. Pucci, "Surface enhanced infrared absorption of octadecanethiol on wet-chemically prepared Au nanoparticle films," *Appl. Phys. Lett.* **88**(18), 184104 (2006).
41. S. Bagheri, H. Giessen, and F. Neubrech, "Large-Area Antenna-Assisted SEIRA Substrates by Laser Interference Lithography," *Adv. Opt. Mater.* **2**(11), 1050–1056 (2014).
42. C. M. Ramos, L. F. Alzate, N. M. Hernández, S. P. Hernández, and N. Mina, "Density functional theory treatment of the structures and vibrational frequencies of 2, 4- and 2, 6-dinitrotoluenes," *J. Mol. Struct. THEOCHEM* **769**(1-3), 69–76 (2006).
43. A. Tittl, A. Leitis, M. Liu, F. Yesilkoy, D. Y. Choi, D. N. Neshev, Y. S. Kivshar, and H. Altug, "Imaging-based molecular barcoding with pixelated dielectric metasurfaces," *Science* **360**(6393), 1105–1109 (2018).